ELSEVIER

Intermetallics 8 (2000) 1111–1118

Intermetallics

www.elsevier.com/locate/intermet

Oxidation resistance and mechanical properties of Laves phase reinforced Cr in-situ composites

M.P. Brady *, J.H. Zhu, C.T. Liu, P.F. Tortorelli, L.R. Walker

Oak Ridge National Laboratory, Oak Ridge, TN 37831-6115, USA

Received 12 March 1999; accepted 15 February 2000

Abstract

Two-phase Cr(X)–Cr_2X (X = Nb, Ta) in-situ composites are of interest for high-temperature applications due to their high melting points and potential for high-temperature strength. A six cycle, 120 h, 1100°C cyclic oxidation screening test was used to evaluate potential for high-temperature oxidation resistance of several Cr(X)–Cr_2X in-situ composites. Alloys based on the Cr–Ta system near the Cr(Ta)–Cr_2Ta eutectic exhibited superior oxidation resistance compared to corresponding alloys based on the Cr–Nb system. The binary Cr–Ta alloys were also found to exhibit a moderate degree of room-temperature fracture toughness, in the range of 9–10 MPa$\sqrt{m}$. It was concluded that the Cr(Ta)–Cr_2Ta alloys are a promising base for future high-temperature intermetallic alloy development efforts. © 2000 Elsevier Science Ltd. All rights reserved.

Keywords: A. Laves phases; A. Multiphase intermetallics; B. Environmental embrittlement; B. Fracture toughness; B. Oxidation

1. Introduction

Intermetallic alloys based on Cr_2X (X = Nb, Ta, Zr, Hf, etc.) type Laves phases are candidate materials for high-temperature (>900°C) applications due to their high melting points and potential for high-temperature strength [1,2]. However, they are also extremely brittle at ambient temperatures [1,2]. One potential solution to the brittleness problem is an in-situ composite composed of a ductile matrix phase to provide toughness, reinforced by the Cr_2X Laves phase for high-temperature strength. Such an approach has been successfully demonstrated in low to intermediate temperature (below 600–800°C) alloy development efforts for ferritic steels reinforced by the Fe_2Ta Laves phase [3] and Cu reinforced by the Cr_2Nb Laves phase [4].

For high-temperature alloy development two general approaches to Laves phase containing in-situ composites have been taken: (1) a Nb (Cr) solid solution based matrix [5–10] and (2) a Cr(X) solid solution based matrix [11–17]. Eutectic reactions exist for the Nb(Cr) and Cr_2Nb Laves phases as well as for many Cr(X) and Cr_2X phases. The existence of a eutectic reaction is advantageous because it provides great opportunity for the formation of a wide variety of microstructures through proper control of processing conditions [16].

Ambient fracture toughness in the range of 20 MPa$\sqrt{m}$ has been achieved for Ti-modified Nb(Cr)–Cr_2Nb in-situ composites [7]. However, although the Nb(Cr,Ti) matrix phase is ductile, it is not oxidation resistant and, further, is likely susceptible to oxygen embrittlement during elevated temperature exposure in air [18]. It is not clear if the environmental durability of this class of materials can be sufficiently improved for use in long-term, high-temperature structural applications.

The rationale behind the selection of a Cr(X) matrix is its potential for improved oxidation resistance due to the formation of a protective Cr_2O_3 scale. The drawback is that although Cr can exhibit appreciable ambient ductility under limited circumstances, under most conditions it is quite brittle at ambient temperatures [19]. Further, Cr can be extensively embrittled by nitrogen during elevated temperature exposure in air [19] although that embrittlement can be limited by additions (e.g. reactive element based dispersions such as Y_2O_3) which improve the adherence and overall protectiveness of the Cr_2O_3 scale [20]. Complete environmental protection from Cr_2O_3 scales (no coating needed) is generally limited

* Corresponding author.
E-mail address: bradymp@ornl.gov (M.P. Brady).

0966-9795/00/$ - see front matter © 2000 Elsevier Science Ltd. All rights reserved.
PII: S0966-9795(00)00046-7

to below about 1000–1100°C (lower in the presence of high flow rates and/or water vapor) due to oxide volatility (e.g. [21]). Despite these limitations, Cr(X)–Cr_2X based in-situ composites offer the possibility for a considerable degree of high-temperature oxidation and embrittlement resistance. The purpose of the present work is to present the results of initial studies of the high-temperature oxidation and room-temperature fracture toughness (two key properties from an alloy development standpoint) of some Cr(X)–Cr_2X based alloys (X = Nb, Ta) of interest for high-temperature structural applications.

2. Experimental

2.1. Alloy preparation

Alloys based on the Cr(Nb)–Cr_2Nb and Cr(Ta)–Cr_2Ta systems (Figs. 1 and 2) [22–24] were prepared by arc melting and drop casting in a chilled copper mold. High-purity Nb and Ta metal chips were used as charge materials. Although the Cr source was commercial-purity it was found to contain significant quantities of impurities [7058 O, 112 N, 200 C, 350 S weight parts per million (wppm)]. Select alloys were recast using high-purity Cr from JMC (USA) which contained 170 O, 20 N, < 100 C, < 10 S wppm. The Cr–Nb and Cr–Ta castings were found to be within ± 0.5 at.% of the nominal Cr, Nb, Ta levels (as measured by inductively coupled plasma spectroscopy and/or electron probe microanalysis). Alloys cast from the commercial-purity Cr typically contained 2000–4000 O, 40–60 N, 100 C, 100–200 S wppm while alloys cast from the high-purity Cr typically contained 100–300 O, < 10 N, < 100 C, < 10 S wppm (as determined by gas fusion).

There was no significant effect of impurity level detected on the oxidation behavior or the room-temperature fracture toughness of the Cr–Ta alloys under the conditions studied. However, a beneficial effect of a high level of impurities was observed for the oxidation of some Cr–Nb alloys, with reduced nitrogen penetration ahead of the oxide scale when Cr_2Nb-based Cr(Nb)–Cr_2Nb alloys made from the commercial-purity Cr were exposed in filtered compressed dry air. This effect was not evident in humid laboratory air, with no significant differences in oxidation behavior observed between Cr–Nb alloys cast with commercial-purity and high-purity Cr. [The role of the impurities during oxidation of Cr(Nb)–Cr_2Nb and Cr(Ta)–Cr_2Ta alloys is currently under investigation.] Unless otherwise noted, the oxidation data are from alloys made with the commercial-purity Cr and the room-temperature fracture toughness data are from alloys made with the high-purity Cr.

2.2. High-temperature oxidation

Disk shaped oxidation specimens of approximately 8–13 mm in diameter and 1 mm in thickness were polished to a 600-grit finish using SiC paper. Short term cyclic oxidation screening tests were performed at 1100°C in a tube furnace open to humid, laboratory air. The samples were placed face down together in a covered alumina crucible (40 mm diameter) and inserted/removed from the furnace at temperature (air cooling) and weighed after intervals of 1, 4, 10, 30, 48, and 120 h of cumulative exposure. As expected for this temperature, there was some chromia volatility as evidenced by green stains on the underside of the alumina crucible lid. However, volatility-related weight loss did not appear to be significant compared to oxidative weight gains under the conditions studied.

Oxidized coupons were characterized by X-ray diffraction (XRD), optical microscopy, secondary mode scanning electron microscopy (SEM), and electron probe microanalysis (EPMA) using pure element standards for Cr, Nb, and Ta; a BN standard for N; and an Al_2O_3 standard for O. Room-temperature Vickers microhardness measurements (100 g, 15 s) were used on polished cross-sections to qualitatively evaluate the hardening associated with nitrogen penetration into the alloy ahead of the alloy–scale interface.

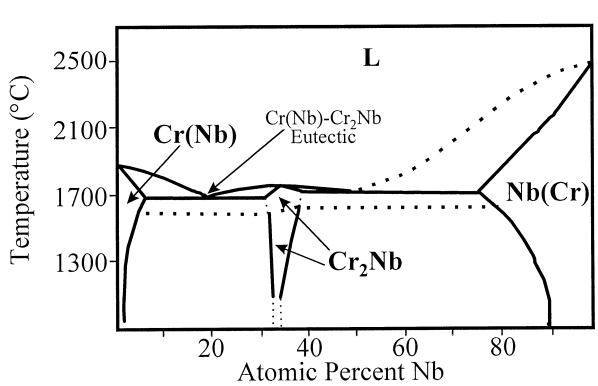

Fig. 1. Schematic Cr–Nb phase diagram based on [22].

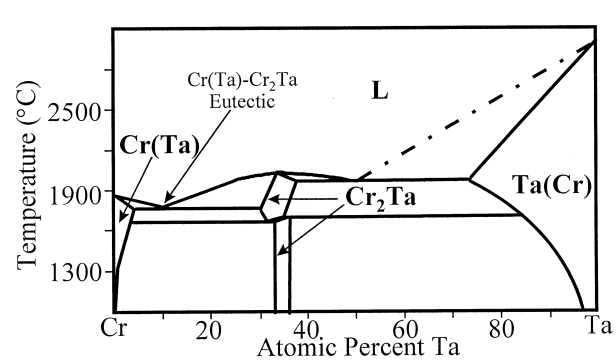

Fig. 2. Schematic Cr–Ta phase diagram based on [23,24].

2.3. Room-temperature fracture toughness

Subsized chevron-notched three-point bend samples approximately 3×4×(20–25) mm were used to evaluate fracture toughness at room-temperature. The cross-head speed was 10 μm/s. A modulus of 250 GPa was estimated for the Cr(Ta)–Cr_2Ta based alloys. Details of this technique are provided in [25].

3. Results

3.1. Oxidation

The 1100°C cyclic oxidation screening data for two as-cast Cr(*X*)–Cr_2X alloys, Cr–10Nb and Cr–10Ta (all compositions in atomic percent) are shown in Fig. 3. For comparative purposes, data for as-cast pure Cr, Cr–9.5Ta cast from high-purity Cr (prior 1300°C, 24 h heat treatment), and Cr–18.5Nb cast from commercial-purity and high-purity Cr (prior 1300°C, 24 h heat treatment) are also shown. Data for Cr–18.5Nb, the Cr(Nb)–Cr_2Nb eutectic composition [22], are shown because Cr–10Ta effectively coincides with the Cr(Ta)–Cr_2Ta eutectic [23] [see Section 3.2 for further details on the Cr(Ta)–Cr_2Ta eutectic]. No significant effect of impurity level under the short term cyclic, humid air exposure conditions presented in Fig. 3 was detected for either the Cr–Nb or Cr–Ta alloys. All of the Cr–Nb alloys and the pure Cr suffered extensive scale spallation, with the Cr sample showing complete scale loss at the conclusion of the test. The Cr–Ta alloys showed no evidence of scale spallation and low weight gains (relative to other Laves phase alloys).

SEM cross-section micrographs of the pure Cr, Cr–10Nb, and Cr–10Ta coupons from the six cycle, 120 h 1100°C cyclic screening test of Fig. 3 are shown in Figs. 4–8. A hardened and embrittled zone ranging from 30 to 50 μm deep was present in the near surface regions of the pure Cr sample (Fig. 4). EPMA analysis of similar samples revealed that this hardening was associated with Cr–nitride formation of a stoichiometry corresponding to the Cr_2N phase (identification based solely on EPMA).

Nearly all of the Cr–10Nb alloy coupon was converted to a complex mixture of Cr–, Nb–, and Cr + Nb–oxides (Fig. 5a). Examination of shorter term exposed Cr–Nb alloys suggested that a continuous outer Cr_2O_3 layer was initially formed on Cr–10Nb but subsequently spalled off during the course of the screening test. Extensive nitride-based subscale formation was evident (Fig. 5b).

The microstructure of Cr–10Nb consisted of primary Cr(Nb) solid solution phase regions containing fine Cr_2Nb phase precipitates surrounded by an interconnected network of the Cr_2Nb Laves phase containing a small volume fraction of the Cr(Nb) phase. The subscale mimicked this microstructure, with the Cr_2Nb Laves phase and the Cr(Nb) phase nitriding independently. EPMA analysis revealed two–distinct layers of subscale formation in Cr–10Nb (regions A and B in Fig. 5b). In the first layer (region A), both the Cr(Nb) and Laves phases were nitrided. Vicker's microhardness measurements showed that this nitridation resulted in extensive hardening (1700 VHN) and embrittlement of the Cr(Nb) phase to a depth of approximately 80–100 μm (Fig. 6), more than double that observed in the pure Cr sample shown in Fig. 4. In the second layer (region B), only the Laves phase was nitrided. The Cr(Nb)

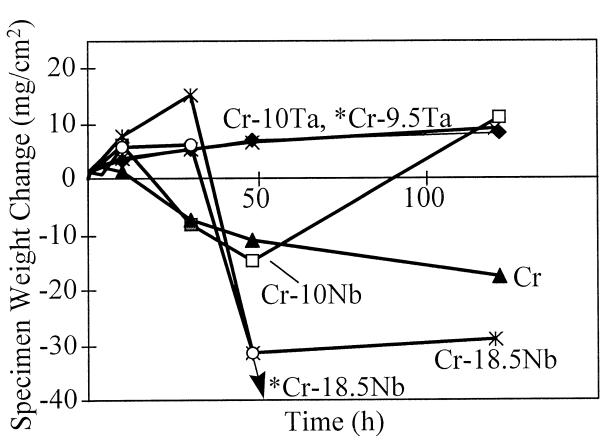

Fig. 3. Cyclic oxidation at 1100°C in humid "laboratory" air. At each data point the sample was air cooled, weighed, and returned to the furnace at temperature (*,sample cast with high-purity Cr).

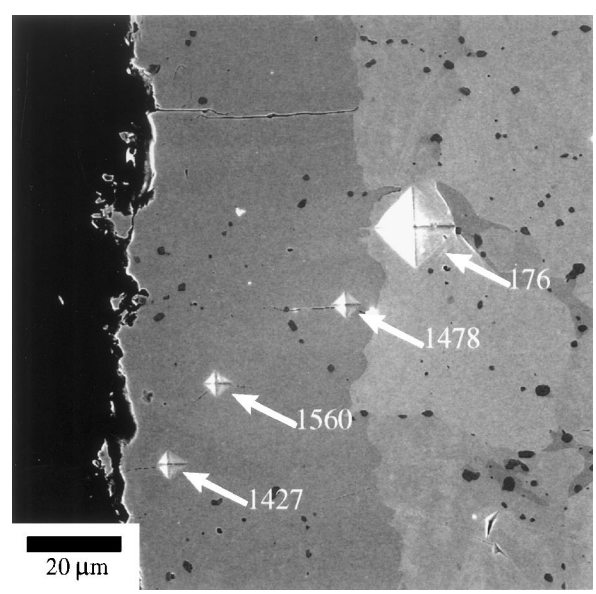

Fig. 4. SEM (secondary electron) cross-section micrograph of pure Cr after the six cycle, 120 h, 1100°C humid air exposure from Fig. 3. The Cr_2O_3 scale completely spalled. Subscale nitridation and embrittlement are evident. The Vicker's microhardness indents and the corresponding values are marked by the arrows. (The dark particles throughout the microstructure are oxide impurity inclusions.)

phase remained metallic. Region B was relatively soft with a composite hardness of ≈ 550 VHN. The depth of selective nitridation of the Cr_2Nb Laves phase was not quantitatively determined. It likely extended throughout the entire sample depth due to overlap of the reaction front from the opposite coupon face, i.e. nearly all of the coupon cross-section was oxidized/nitrided (Fig. 5a). (The microstructure of oxidized Cr–18.5Nb was qualitatively similar to that observed for Cr–10Nb.)

A continuous, adherent outer Cr_2O_3 layer approximately 15–20 μm thick was formed on Cr–10Ta after the 6 cycle, 120 h 1100°C screening test (Figs. 7 and 8). Underlying the Cr_2O_3 layer was an inner oxide-based layer of similar thickness (region A in Fig. 7) which consisted of a predominately oxide phase of a compositional stoichiometry corresponding to $CrTaO_4$ (light phase) and a nitride phase of a stoichiometry corresponding to Cr_2N (dark phase). (Phase identification based solely on EPMA data). As with Cr–10Nb, a subscale which mimicked the underlying alloy microstructure was also formed (region B in Fig. 7). It contained a nitride phase derived from selective attack of the Cr_2Ta phase, while the Cr(Ta) phase in this region remained metallic. The depth of selective nitridation of the Cr_2Ta Laves phase in region extended approximately 100 μm beyond the region A/B interface. Vickers microhardness measurements showed no evidence of hardening in region B, which is consistent with the EPMA measurements which showed that the Cr(Ta) matrix in this region was not nitrided (Figs. 7 and 8).

The presence of a small quantity of nitrogen in the $CrTaO_4$ phase in region A suggests that it formed from the oxidation of the nitrided Cr_2Ta phase in region B (Fig. 7). Similar nitrogen containing oxide phases were observed in the external scale in Cr–10Nb near the external scale/region A interface (Fig. 5b). Qualitatively,

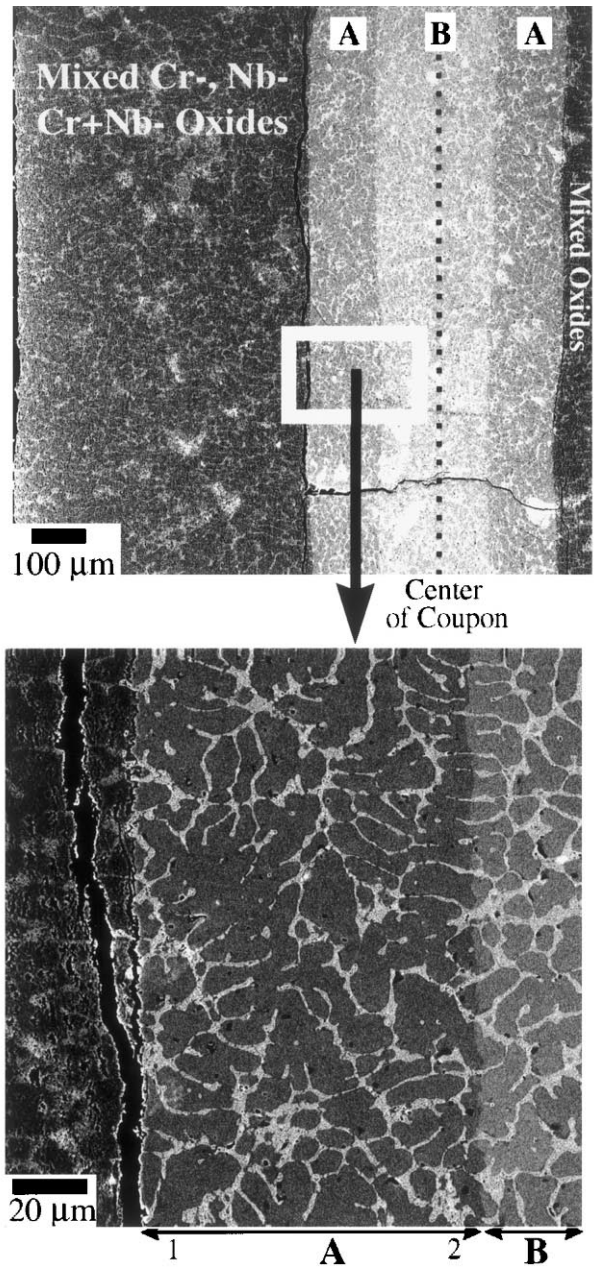

Former Cr(Nb) Phase Location (dark)	Composition (at.%)	Former Cr_2Nb Phase Location (light)	Composition (at.%)
A-1	58Cr-2Nb-40N	A-1	40Cr-23Nb-37N
A-2	65Cr-3Nb-32N	A-2	46Cr-22Nb-32N
B	97Cr-3Nb	B	54Cr-25Nb-21N
Bulk	98Cr-2Nb	Bulk	68Cr-32Nb

Fig. 5. EPMA data (rounded to nearest 1 at.%) and SEM (secondary electron) cross-section micrographs of Cr–10Nb after the six cycle, 120 h, 1100°C humid air exposure from Fig. 3: (a) overview, (b) scale/subscale interface region.

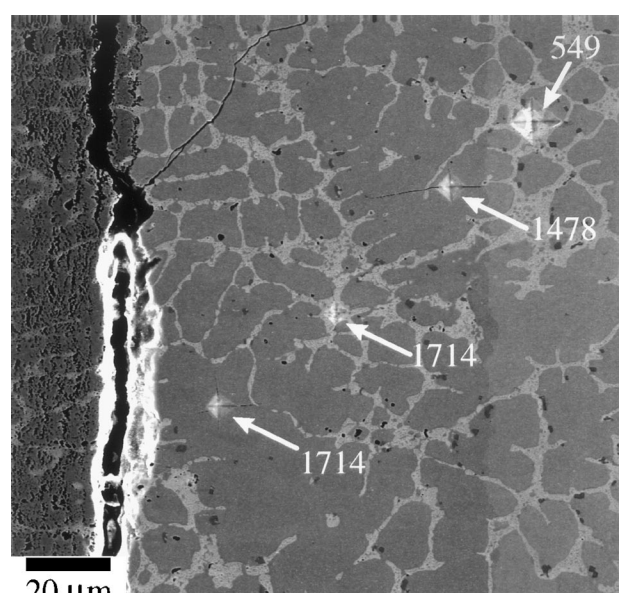

Fig. 6. SEM (secondary electron) cross-section micrograph of the scale/subscale interface in oxidized Cr–10Nb from Fig. 5b showing subscale embrittlement. The Vicker's microhardness indents and the corresponding values are marked by the arrows.

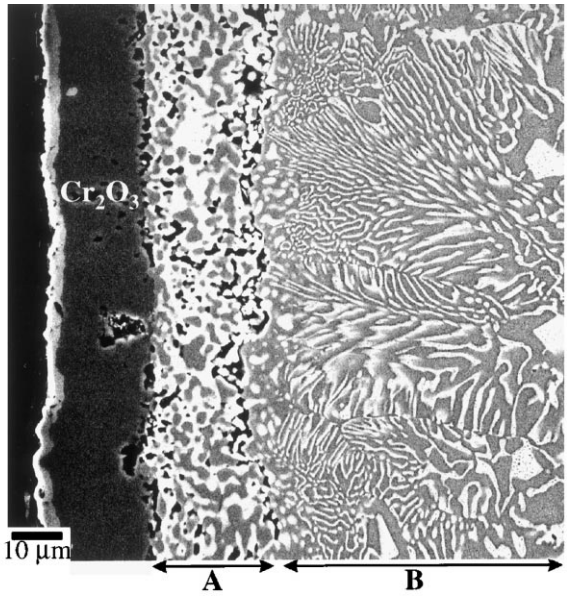

Former Cr(Ta) Phase Location (dark)	Composition (at.%)	Former Cr_2Ta Phase Location (light)	Composition (at.%)
A	67Cr-33N	A	18Cr-19Ta-60O-4N
B	99Cr-1Ta	B	51Cr-22Ta-27N
Bulk	99Cr-1Ta	Bulk	67Cr-33Ta

Fig. 7. EPMA data (rounded to nearest 1 at.%) and SEM (secondary electron) cross-section micrograph of Cr–10Ta after the six cycle, 120 h, 1100°C humid air exposure from Fig. 3. Note that the bright layer at the outer edge of the Cr_2O_3 scale is an artifact.

there appeared to be a higher percentage of the $CrTaO_4$ phase in region A than what would be predicted from a direct 1:1 conversion from the nitrided Cr_2Ta Laves phase from region B (which matched the volume fraction of the Laves phase in the bulk alloy). This suggests an initial period of selective Cr consumption to form the outer Cr_2O_3 layer, which resulted in a local increase in the relative volume fraction of the Cr_2Ta Laves phase at the expense of the Cr(Ta) phase. Some porosity was also evident in layer A, which is consistent with preferential outward diffusion of Cr. However, at least some of this porosity possibly resulted from pullout during metallographic preparation.

3.2. Room-temperature fracture toughness

Based on the promising oxidation behavior of Cr–10Ta (and the poor behavior of Cr–10Nb and Cr–18.5Nb) only binary Cr–Ta alloys were evaluated for room-temperature fracture toughness. The Cr(Ta)–Cr_2Ta eutectic was found to occur between approximately 9.5 and 10 at.% Ta (Fig. 9) [23], which is at a lower Ta level than the currently accepted Cr–Ta phase diagram which shows this eutectic composition at approximately 13 at.% Ta [24]. Three alloys were selected based on the Cr–(9.5–10Ta) eutectic location: hypoeutectic Cr–8Ta, approximate eutectic Cr–9.8Ta, hypereutectic Cr–11Ta. The

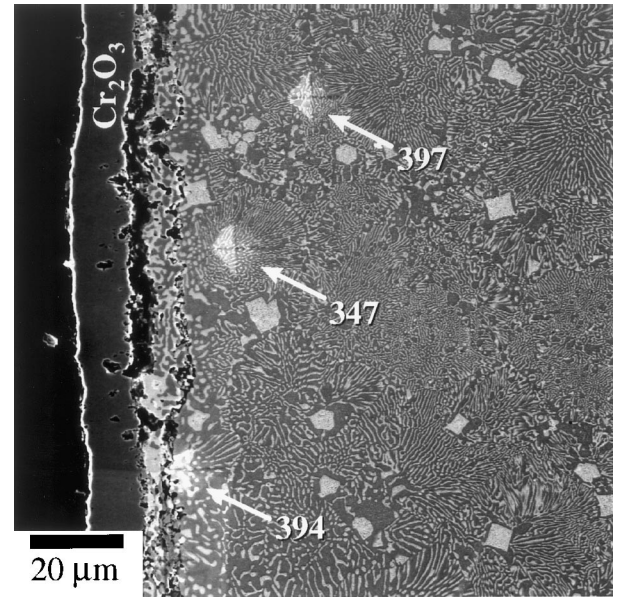

Fig. 8. SEM (secondary electron) cross-section micrograph of oxidized Cr–10Ta from Fig. 7 showing resistance to subscale embrittlement. The Vicker's microhardness indents and the corresponding values are marked by the arrows.

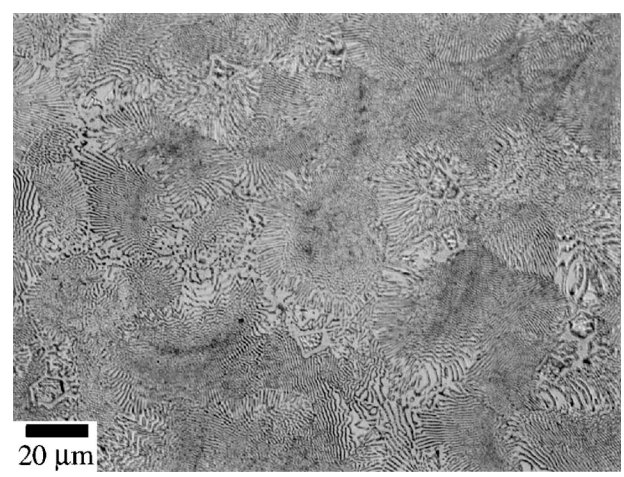

Fig. 9. Optical light micrograph of as-cast Cr–9.7Ta showing a nearly 100% eutectic microstructure.

alloys were cast from the high-purity Cr and then heat-treated at 1000°C for 24 h (furnace cool).

The fracture toughness values ranged between approximately 9–10 MPa$\sqrt{m}$ and were independent of composition in this range (Table 1). For comparative purposes, several samples of Cr–9.7 Ta were cast from the commercial-purity Cr and heat-treated at 1000°C for 24 h as before. One sample broke during loading, a second failed outside of the notched region and yielded a fracture toughness value of 5.1 MPa$\sqrt{m}$, the third sample broke at the notched region and yielded a fracture toughness value of 9.1 MPa$\sqrt{m}$, a similar value to that measured in the Cr–Ta alloys cast from the high-purity Cr. The high level of impurities associated with the

Table 1
Chevron-notched fracture toughness at room temperature

Alloy	Fracture toughness (MPa$\sqrt{m}$)
Cr–8Ta	9.4, 9.5, 10.5
Cr–9.8Ta	8.9, 9.0
Cr–11Ta	9.6, 9.8

commercial-purity Cr therefore appears to have little inherent detrimental effect on room-temperature fracture toughness, with the possible exception of impurity-based inclusions (e.g. oxide particles) acting as local flaws.

The fracture surface morphology was found to mimic the underlying alloy microstructures. Brittle cleavage fracture was observed in the primary Cr(Ta) regions in Cr–8Ta (Fig. 10a) and in the primary Cr_2Ta regions in Cr–11Ta (Fig. 10b). The lamellar Cr(Ta)–Cr_2Ta eutectic regions in all three alloys showed a relatively flat fracture surface, indicating strong bonding between the Cr(Ta) and Laves phases.

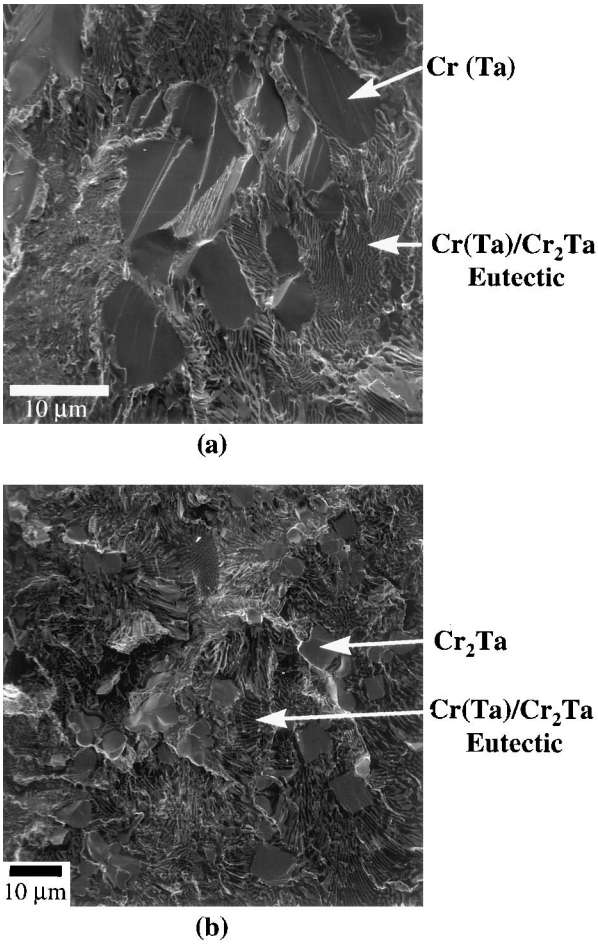

Fig. 10. SEM (secondary electron) fractographs of select chevron-notched fracture toughness samples from Table 1: (a) Cr–8Ta, (b) Cr–11Ta.

4. Discussion

The Cr–10Ta alloy exhibited oxidation resistance superior to Cr–10Nb, Cr–18.5Nb, and pure Cr in the simple six cycle, 120 h 1100°C air cyclic oxidation screening test used in this study. The poor behavior of the pure Cr is not surprising as it is well established that during high-temperature oxidation in air pure Cr forms a highly buckled, poorly adherent Cr_2O_3 scale [26]. However, given the general similarities of Nb and Ta, it is surprising that the oxidation resistance of Cr–10Nb was significantly worse than that of Cr–10Ta.

The scale and subscale features formed on Cr–10Nb were qualitatively similar to those formed on Cr–10Ta, despite the great difference in the extent of attack. The major difference is that the scale formed on Cr–10Ta appears to be much less permeable to nitrogen than the scale formed on Cr–10Nb. The reasons for this are not readily apparent and are the subject of ongoing work. However, preliminary oxidation studies of single phase Cr(X) and Cr_2X alloys suggest that the Cr(Ta) phase is more nitridation resistant than the Cr(Nb) phase, possibly because the lower solubility of Ta in Cr than Nb ($\approx$ 0.6 vs 1.5 at.% in the 1100–1300°C range) may lead to the formation of a more protective Cr_2O_3 scale [27]. The Cr_2X Laves phase is also much less oxidation-resistant than the Cr(X) phase, and the Cr(Ta)–Cr_2Ta eutectic contains much less Cr_2X phase than the Cr(Nb)–Cr_2Nb eutectic (compare Figs. 1 and 2) [27].

A key finding of this work was that the Cr_2X Laves phase in both alloys was nitrided to a much greater depth than the Cr(X) phase. This was a contributing factor to the relative lack of nitrogen embrittlement of the Cr(Ta) phase in Cr–10Ta (Figs. 7 and 8). The Cr_2Ta Laves phase acted as a sink for nitrogen and effectively gettered the relatively small (compared to pure Cr and Cr–10Nb) flux of nitrogen that passed through the scale. Because it is already quite brittle, nitridation of the Laves phase is unlikely to significantly degrade the toughness of the alloy. However, as evidenced by the extensive embrittlement in Cr–10Nb, if the scale becomes highly permeable to nitrogen the beneficial gettering effect of the Laves phase can be overwhelmed.

The parabolic rate constant for Cr–10Ta derived from the 120 h, 1100°C cyclic oxidation screening weight gain data is estimated to be on the order of 2×10^{-10} g^2 cm^{-4} s^{-1} (note that there was a strong linear component to the data and that the r^2 values for the parabolic fit typically ranged from 0.9 to 0.95). This rate is within 3 orders of magnitude of a "good" protective Al_2O_3-forming alloy and 2 orders of magnitude of the best reactive element doped Cr_2O_3-forming alloys [28]. However, it is important to point out that limited (in progress) studies of long-term (up to 10×100 h cycles, 1000 total hours) exposures of reactive element (La or Y) + Si micro-alloyed Cr-Ta alloys suggest that the rate

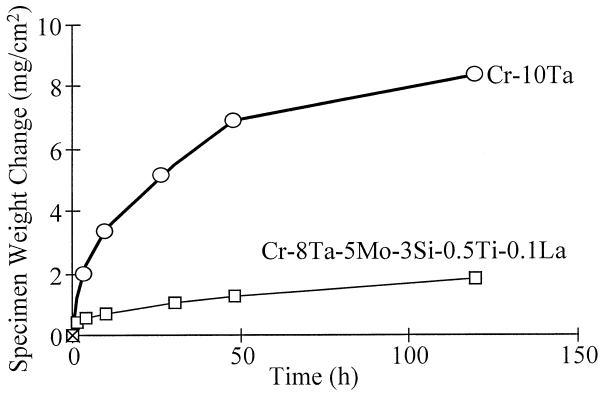

Fig. 11. Cyclic oxidation at 1100°C in humid "laboratory" air. At each data point the sample was air cooled, weighed, and returned to the furnace at temperature. The Cr–8Ta–5Mo–3Si–0.5Ti–0.1La alloy was cast using the high-purity Cr, HiPed at 1530°C, and then heat-treated at 1000°C for 48 h.

of oxidation at 1100°C can be reduced up to an additional order of magnitude [29] (Fig. 11). Further, the extent of nitrogen penetration in these alloys is less than that observed in Cr–10Ta.

From a design standpoint, a minimum room-temperature fracture toughness of at least 15–20 MPa$\sqrt{m}$ and preferably greater than 20–25 MPa$\sqrt{m}$ is desired for most structural applications. The binary Cr(Ta)–Cr_2Ta alloys are roughly halfway to this point. Fractography of the room-temperature chevron-notched fracture toughness samples (Fig. 10) revealed little debonding between the Cr(Ta) and Cr_2Ta phases in the lamellar eutectic regions of the microstructure. This suggests alloying to weaken the Cr(Ta)/Cr_2Ta interface as one approach to improve fracture toughness. Given that, at room temperature, the primary Cr(Ta) regions exhibited brittle cleavage fracture, alloying additions aimed at increasing the ambient ductility of Cr would also improve fracture toughness. Efforts devoted to both approaches are currently underway [29].

5. Summary

The preliminary results of this study suggest that in-situ composites based on the Cr(Ta)–Cr_2Ta eutectic are attractive for development as a potential high-temperature alloy due to a promising combination of a moderate degree of high-temperature oxidation and embrittlement resistance and room-temperature fracture toughness. Specifically:

1. A Cr(Ta)–Cr_2Ta in-situ composite alloy, Cr–10Ta, exhibited a parabolic rate constant on the order of 2×10^{-10} g^2 cm^{-4} s^{-1} in a six cycle, 120 h, 1100°C cyclic oxidation screening in humid air. Under the same conditions, comparable Cr(Nb)–Cr_2Nb based alloys suffered from rapid oxidation and extensive scale spallation. Selective nitridation of the Cr_2Ta Laves phase ahead of the alloy/scale interface in Cr–10Ta limited the extent to which the Cr(Ta) matrix phase was embrittled by nitrogen.
2. Binary Cr(Ta)–Cr_2Ta in-situ composites in the range of Cr–(8–11)Ta exhibited room-temperature fracture toughness values in the range of 9–10 MPa$\sqrt{m}$.

Acknowledgements

The authors thank C.A. Carmichael, E. Lee, and J.L. Wright for their technical assistance in the preparation and characterization of these alloys. The authors also thank Ian Wright and Joachim Schneibel for helpful comments on this manuscript. JMC (USA) donated high-purity Cr for this study. This research was sponsored by the Fossil Energy Advanced Research and Technology Development (AR&TD) Materials Program, US Department of Energy, under contract DE-AC05-96OR22464 with Lockheed Martin Energy Research Corporation. The submitted manuscript has been authored by a contractor of the US Government under contract No. DE-AC05-96OR22464. Accordingly, the US Government retains a nonexclusive, royalty-free license to publish or reproduce the published form of this contribution, or allows others to do so for US Government purposes.

References

[1] Livingston JD. In: Briant CL, Petrovic JJ, Bewlay BP, Vasudevan AK, Lipsitt HA, editors. High-temperature silicides and refractory alloys. Pittsburgh (PA): MRS, 1994. p. 395–406.
[2] Kumar KS. In: Koch CC, Liu CT, Stoloff NS, Wanner A, editors. High-temperature ordered intermetallic alloys VII. Pittsburgh (PA): MRS, 1997 p. 677–688.
[3] Bhandarkar MD, Bhat MS, Parker ER, Zackay VF. Metal Trans A 1975;7A:753–60.
[4] Anderson KR, Groza JR, Dreshfield RL, Ellis D. Metall Mater Trans A 1995;26(9):2197–206.
[5] Bewlay BP, Sutliff JA, Jackson MR, Lipsitt HA. Acta Metal Mater 1994;42(8):2869–78.
[6] Shah DP, Anton DL, Pope DP, Chim S. Mater Sci Eng A 1995;A192/193:658–72.
[7] Chan KS, Davidson DL. JOM 1996;9:62–7.
[8] Chan KS. Metall Mater Trans A 1996;27A:2518–31.
[9] Jackson MR, Bewlay BP, Rowe RG, Skelly DW, Lipsitt HA. JOM 1996;1:39–44.
[10] Chen KC, Thoma DJ, Chu F, Kotula PG, Cady CM, Gray III GT et al. In: Proceedings of the Third Pacific Rim International Conference on Advanced Materials and Processing (PRICM 3), 1998. 1431–1437.
[11] Takeyama M, Liu CT. Mater Sci Eng A 1990;A132:61–6.
[12] Liu CT, Tortorelli PF, Horton JA, Carmichael CA. Mater Sci Eng A 1996;A214:23–32.
[13] Kumar KS, Liu CT. Acta Mater 1997;45(9):3671–86.
[14] Aoyama N, Hanada S. Mater Trans JIM 1997;38(2):155–62.
[15] Yoshida M, Takasugi T. Mater Sci Eng A 1997;224(1-2):77–86.

[16] Mazdiyasni M, Miracle DB. In: Anton DL, Martin PL, Miracle DB, McMeeking R, editors. Intermetallic matrix composites. Pittsburgh (PA): MRS, 1990. p. 155–162.
[17] Ravichandran KS, Miracle DB, Mendiratta MG. Metall Mater Trans A 1996;27A:2583–92.
[18] Brady MP, Pint BA, Tortorelli PF, Wright IG, Hanrahan Jr RJ, High-temperature oxidation and corrosion of intermetallics. In: Schutze M, editor. Corrosion and environmental degradation of materials. Weinheim (Germany): Wiley-VCH, 2000, p. 229–325.
[19] Scully AH, Brandes EA. Chromium 2nd ed. New York: Plenum Press: Edition, 1967, p. 161–210.
[20] Lawn RE, Wilson FG, Desforges CD. J Less-Common Metal 1978;58:107–10.
[21] Opila EJ, Jacobson NS. In: Shores DA, Rapp RA, Hou PY, editors. Fundamental aspects of high temperature corrosion. Pennington (NJ): The Electrochemical Society, 1997. p. 269–280.
[22] Thoma DJ, Perepezko JH. Mater Sci Eng 1992; A156:97.
[23] Zhu JH, Liu CT. Oak Ridge National Laboratory, unpublished results, 1997.
[24] Venkatraman M, Neumann JP. In: Massalaski TB, Murray JL, Bennett LH, Baker H, editors. Binary alloy phase diagrams, vol. 1, ASM, 1986. p. 867.
[25] Schneibel JH, Carmichael CA, Specht ED, Subramanian R. Intermetallics 1997;5:61–7.
[26] Kofstad P. High temperature corrosion. London: Elsevier Applied Science Publishing, 1988.
[27] Brady MP, Tortorelli PF, Walker LR. Materials at High Temperatures, 17(2), in press.
[28] Hindam H, Whittle DP. Oxidation of metals 1982;18(5/6):245.
[29] Brady MP, Zhu JH, Liu CT, Tortorelli PF, Walker LR, McKamey CG, et al. Materials at High Temperatures 1999;16(4):189–93.